International Journal of Multiphase Flow 56 (2013) 172–183

Contents lists available at SciVerse ScienceDirect

International Journal of Multiphase Flow

journal homepage: www.elsevier.com/locate/ijmulflow

Particle and droplet deposition in turbulent swirled pipe flow

Francesco Zonta, Cristian Marchioli, Alfredo Soldati *

Centro Interdipartimentale di Fluidodinamica e Idraulica, Università degli Studi di Udine, Udine, Italy
Department of Fluid Mechanics, CISM, 33100 Udine, Italy

ARTICLE INFO

Article history:
Received 25 March 2013
Received in revised form 7 June 2013
Accepted 8 June 2013
Available online 17 June 2013

Keywords:
Turbulence
Swirling flows
Numerical simulation
Lagrangian tracking

ABSTRACT

In this work we study deposition of particles and droplets in non-rotating swirled turbulent pipe flow. We aim at verifying whether the capability of swirl to enhance particle separation from the core flow and the capability of turbulence to efficiently trap particles at the wall can co-exist to optimize collection efficiency in axial separators. We perform an Eulerian–Lagrangian study based on Direct Numerical Simulation (DNS) of turbulence, considering the effect of different swirl intensities on turbulence structures and on particle transfer at varying particle inertia. We show that, for suitably-chosen flow parameters, swirl may be superimposed to the base flow without disrupting near-wall turbulent structures and their regeneration mechanisms. We also quantify collection efficiency demonstrating for the first time that an optimal synergy between swirl and wall turbulence can be identified to promote separation of particles and droplets.

1. Introduction

In-line separation of particles and droplets (simply referred to as particles hereinafter) from a gas stream is an important problem in many engineering applications, such as dedusting and demisting in process, oil and gas industries (Peng et al., 2004; Klujszo et al., 1999; Soldati et al., 1997). A widely used solution is to exploit the larger inertia of particles and propel them toward the wall via a suitable rotating motion of the mean flow. This motion can be generated by changes in flow geometry, as for instance by static vanes in axial separators for gas cleaning (Peng et al., 2004; Gomez et al., 2004), or by curved ducts in gas-cleaning cyclones and in hydro-cyclones for separation of liquid–liquid mixtures (Delfos et al., 2004).

In this work we address the problem of gas–solid/gas–liquid separation in axial tubes equipped with swirl vanes (swirl tubes, see Nieuwstadt and Dirkzwager, 1995). Design of such devices crucially depends on the interactions among swirling motions, near-wall turbulence and particles, which give rise to complex dynamics that involve turbulence forcing by swirl, and may have a strong effect on the near-wall turbulence regeneration mechanisms. Previous studies (Orlandi and Fatica, 1997; Eggels, 1994; Pettersson et al., 1998) have shown that swirling motions induced by a pipe rotating about its axis can influence turbulence to the point of flow re-laminarization. Such findings promoted a large effort dedicated to identify sustainable strategies for drag reduction by interrupting turbulence regeneration cycle, ultimately disrupting wall structures. However, the very same wall structures found detrimental for drag reduction are found beneficial for particle separation by enhancing deposition and wall trapping (Marchioli and Soldati, 2002; Soldati, 2005; Soldati and Marchioli, 2009). Therefore, for optimal separation design, characteristics of swirl and wall structures should be tuned to ensure fast transfer to the wall (due to swirl-induced centrifugation) and efficient trapping (due to turbulence-induced preferential concentration): once confined in the wall layer, particles may be removed using suction slots or similar filtration systems (Nieuwstadt and Dirkzwager, 1995).

Many detailed numerical (Orlandi and Fatica, 1997; Eggels, 1994; Pettersson et al., 1998) and experimental (Kitoh, 1991; Steenbergen and Voskamp, 1998; Parchen and Steenbergen, 1998; Pashtrapanska et al., 2006) studies on swirl-induced turbulence modification are available. However, most of them focus on drag reduction application and hence examine swirling motions generated by a rotating pipe wall (see Speziale et al., 2000 for a review) or by an imposed circumferential pressure gradient (Nygard and Andersson, 2010). The influence of swirl on turbulence is less clear when it is produced in the core of the pipe, e.g. by static tilted vanes. These two instances of swirled flow have a fundamental difference: swirl is centripetal in rotating pipes, where it leads to transport of vorticity and displacement of vortices away from the wall, but centrifugal in swirled tubes. Evidence of boundary layer thickening for centripetal swirl has been demonstrated (Orlandi and Fatica, 1997; Eggels, 1994). For centrifugal swirl we may hypothesize a qualitatively correspondent boundary layer thinning, which however was not investigated in detail previously.

* Corresponding author at: Centro Interdipartimentale di Fluidodinamica e Idraulica, Università degli Studi di Udine, Udine, Italy. Tel.: +39 0432 558020; fax: +39 0432 558027.
E-mail address: soldati@uniud.it (A. Soldati).

0301-9322/$ - see front matter © 2013 Elsevier Ltd. All rights reserved.
http://dx.doi.org/10.1016/j.ijmultiphaseflow.2013.06.002

The first objective of this work is therefore to analyze the flow field in an axial swirl tube separator. We know from literature that (i) swirl is beneficial in quickly propelling particles to the wall (Kitoh, 1991; van Esch and Kuerten, 2008); (ii) wall turbulence is efficient in trapping particles at the wall (Marchioli and Soldati, 2002; Soldati, 2005); and (iii) high swirl intensity can destroy near-wall turbulence structures (Orlandi and Fatica, 1997; Eggels, 1994): here, we want to assess the possibility of tuning swirl characteristics to prevent disruption of near-wall structures due to excessive centrifugal forcing. This is relevant for real-life separation devices, e.g. vertical separators, where near-wall turbulence and not just centrifugation is crucial for separation. Second objective is to examine the behavior of particles and droplets in such flow field, focusing on separation and collection efficiency. Few studies on similar problems are available, which were recently performed by Kuerten and co-workers (Kuerten et al., 2005; van Esch and Kuerten, 2008), albeit for the case of rotational phase separators, where swirl is generated using a rotating cylindrical filter element.

For both objectives, we performed an Eulerian–Lagrangian parametric study of particle dispersion in swirled pipe flow via Direct Numerical Simulation (DNS) of turbulence. DNS ensures the most accurate numerical prediction of particle trajectories. This is a crucial aspect when evaluating separation processes. As demonstrated by Marchioli et al. (2008a), Large Eddy Simulation (LES) is not yet a full alternative to DNS for two-phase flow simulations: Because of filtering, an intrinsic feature of LES, proper modeling of subgrid turbulence is required in the equation of particle motion to avoid time-accumulating filtering errors on trajectories and consequent underestimation of separation efficiency. Such models, however, are currently unavailable (Bianco et al., 2012).

To our knowledge, this is the first fundamental study based on DNS of particle-laden swirled flow in a non-rotating pipe. Results discussed in this paper provide a proof of concept, based on sound physical arguments, that the synergy between swirl-induced centrifugal mechanisms and turbulence-induced trapping mechanisms can be exploited to enhance particle separation in bounded turbulent flows. Though fundamental, this study has strong applicative implications since the flow configuration mimics the behavior of a swirl tube.

2. Problem formulation and numerical methodology

The physical problem investigated in this work considers turbulent flow of air (with density $\rho = 0.965$ kg/m^3 and kinematic viscosity $\nu = 1.57 \times 10^{-5}$ m^2/s) in a pipe with radius $R = 0.025$ m. The flow Reynolds number is $Re = U_{cP}R/\nu = 5000$ with $U_{cP} = 3.14$ m/s the centerline velocity of the laminar Poiseuille flow. The corresponding shear Reynolds number is $Re_\tau = u_\tau R/\nu = 171$ with $u_\tau = \sqrt{\tau_w/\rho} \simeq 0.108$ m/s the shear velocity (τ_w being the mean shear stress at the wall). These values match those considered in previous numerical studies dealing with the same flow configuration (Nygard and Andersson, 2010; Kuerten et al., 2005; van Esch and Kuerten, 2008; Orlandi and Fatica, 1997; Eggels, 1994). The flow configuration is sketched in Fig. 1 together with the cylindrical reference frame. The computational domain consists of an upstream pipe that has axial length $L = 10R$, followed by a downstream pipe of equal radius and length $L = 20R$, in which the swirling motion takes place. For both pipes turbulence is simulated using $N_r \times N_\theta \times N_z = 88 \times 129 \times 129$ (resp. 257) nodes in the radial, azimuthal and axial directions, respectively. Nodes are equally spaced in z and θ, with non-uniform radial refinement (hyperbolic tangent method) close to the wall. The grid resolution is $\Delta z^+ = 13.3$ in the axial direction, while it ranges from $(r \cdot \Delta\theta)^+_{min} = 0.028$ to $(r \cdot \Delta\theta)^+_{max} = 8.25$ in the circumferential direction. The first grid node away from the wall is located at $r^+ = 0.42$, ensuring a resolution sufficient to describe all flow length scales, the Kolmogorov length scale being equal to approximately 1.85 wall units (Marchioli et al., 2003). The time step size is $dt^+ = 0.0117$, sufficient to cope with stability requirements (Courant number restriction). No-slip and no-cross boundary conditions are enforced at the pipe wall for the fluid velocity components.

The numerical method proposed by Verzicco and Orlandi (1996) was adopted for the simulation of both pipes, with the obvious specification of different inlet/outlet boundary conditions. This method solves for the continuity and Navier–Stokes equations in cylindrical coordinates (not shown here for brevity) using a second-order finite-difference discretization for the spatial derivatives, while time derivatives are computed using a third-order low-storage Runge–Kutta scheme for the non-linear terms and an implicit Crank–Nicholson scheme for the viscous terms. The pressure–velocity coupling is handled using a fractional step method which ensures incompressibility at each substep of the Runge–Kutta scheme. Code validation can be found in Marchioli et al. (2003). Flow statistics up to second order show excellent agreement with those of Eggels et al. (1994) and Fukagata and Kasagi (2002). Variables are expressed in outer units, obtained using R and U_{cP} as reference length and velocity for normalization. The corresponding space and time scales are $\mathcal{L} = R$ and $\mathcal{T} = R/U_{cP}$, respectively. In the following, we will also refer to variables expressed in wall units, which will be identified by superscript "+". Wall units are obtained using $\mathcal{L} = \nu/u_\tau$ and $\mathcal{T} = \nu/u_\tau^2$ for normalization.

To reproduce the axially-decaying spin imparted to the fluid through the inclined vanes in swirl tubes, DNS of spatially-developing turbulent flow in the downstream pipe is performed. Inflow conditions for the fluid velocity are obtained from an auxiliary DNS of swirl-free particle-free periodic flow in the upstream pipe: Fully-developed fluid velocity profiles at the outlet section of the periodic flow domain (indicated as u_θ^{PPF} hereinafter) are superimposed to a prescribed Batchelor Vortex (BV) profile (Muntean et al., 2005) which mimics the swirling motion imparted by the tube vanes. The BV produces a centrifugal (rather than centripetal) forcing on the flow and is characterized by the following azimuthal velocity:

$$u_\theta^{BV}(r) = \frac{\Omega R_c^2}{r}\left[1 - \exp\left(-\frac{r^2}{R_c^2}\right)\right], \tag{1}$$

which depends on two parameters: the characteristic angular velocity of the vortex, Ω, and the characteristic vortex radius, R_c, a measure of the vortex core radial extent. This type of swirl, which is not boundary-driven and generates a rotating fluid core of axially-decaying intensity, was investigated in several experimental studies (Kitoh, 1991; Steenbergen and Voskamp, 1998; Parchen and Steenbergen, 1998) at Reynolds numbers much higher than those considered here. The only numerical work we are aware of was performed by Muntean et al. (2005) who, however, used a Reynolds stress model to simulate turbulence and a $k-\epsilon$ model to specify inlet turbulent quantities. The resulting velocity distribution at the inlet of the spatially-developing flow domain is:

$$u_\theta(r, \theta, z = 0, t) = u_\theta^{PPF}(r, \theta, t) + u_\theta^{BV}(r). \tag{2}$$

The present approach proved to be highly accurate, with little or no adjustment of the solution near the inlet boundary and no transient convected downstream (Lund et al., 1998; Sbrizzai et al., 2009). In this study, we fixed $R_c = 0.003$ m and considered three different values for Ω yielding different values of the swirl number S (defined as ratio of axial flux of angular momentum to axial flux of axial momentum): $\Omega_0 = 0$ s^{-1}, corresponding to the swirl-free motion (referred to as $S_0 = S(\Omega_0) = 0$ case); $\Omega_L = 375$ s^{-1}, corresponding to

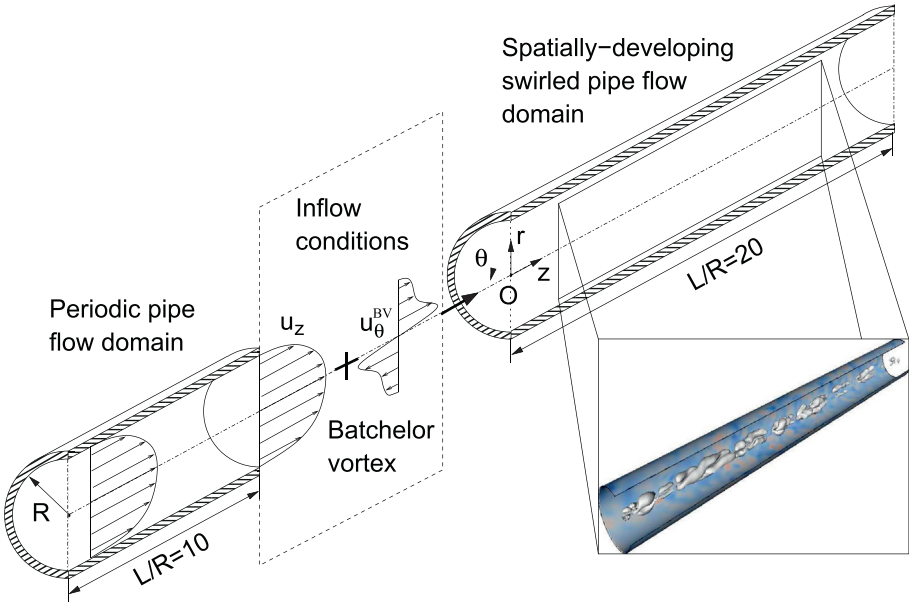

Fig. 1. Sketch of the computational domain. The inset shows the rotating fluid core generated by the swirl in the pipe center, visualized using pressure isosurfaces.

a steady swirling motion with maximum azimuthal velocity $u^{BV}_{\theta,max}(r=R_c)=0.72$ m/s; and $\Omega_H=750\ s^{-1}$, corresponding to $u^{BV}_{\theta,max}(r=R_c)=1.44$ m/s. These two latter cases are referred to as Low-Swirl ($S_L=S(\Omega_L)=0.085$) and High-Swirl ($S_H=S(\Omega_H)=0.17$) hereinafter and the corresponding u^{BV}_{θ}-profiles are shown in Fig. 2: lines represent the theoretical BV profile given by Eq. (1), symbols represent the actual BV profiles considered in our simulations. Brackets denote averaging in space (over θ and z) and time. We remark that Eq. (1) needs a correction to cope with the no-slip condition at the wall: in this work we adopted a quadratic correction, which is highlighted in the inset of Fig. 2. Deviations of the actual BV profile from the theoretical one occur within a fluid layer of five viscous units thickness close to the pipe wall, as indicated by the arrow. The relative strength of the present swirl cases compared with situations where swirl is generated by a rotating pipe wall, can be quantified by means of the rotation number: $N=2\Omega R_c/U_{cP}$, where $R_c=R$ and $\Omega=u_{\theta,max}(r=R)\cdot R^{-1}$for a rotating pipe. Present simulations have $N\simeq 0.5$ (resp. $N\simeq 1$) for the S_L (resp. S_H) case. These values are very close to those considered in several previous

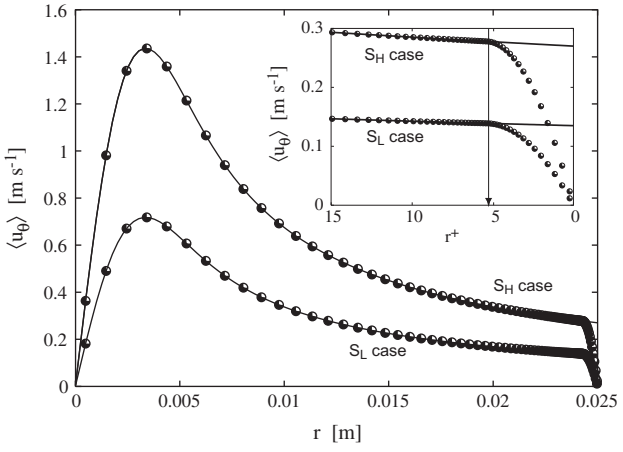

Fig. 2. Mean azimuthal fluid velocity, $\langle u_\theta\rangle$, in physical units at varying swirl strength. Line: analytical Batchelor Vortex (BV) profile; symbols: corrected BV vortex profile. The inset shows a close-up view of the BV profiles near the pipe wall: wall distance is expressed in viscous units ($r^+=rv/u_\tau^2$).

studies, e.g. $0.5\leqslant N\leqslant 2$ in Orlandi and Fatica (1997) and $0.45\leqslant N\leqslant 0.85$ in Nygard and Andersson (2010). Higher values of N ($N>2$) could lead to swirl-induced flow re-laminarization (Eggels, 1994) and are not of interest for our purposes.

At the outlet section, a standard convective condition is applied:

$$\frac{\partial u_i}{\partial t}+U_c\frac{\partial u_i}{\partial n}=0, \tag{3}$$

where $\partial\cdot/\partial n$ is the gradient normal to the boundary while U_c is a convective outflow velocity normal to the boundary. In our simulations, this velocity is set equal to the mean streamwise (bulk) velocity:

$$U_c=U_b=\frac{1}{\pi R^2}\int_0^{2\pi}\int_0^R u_z r\,d\theta dr=\frac{U_{cP}}{2}. \tag{4}$$

2.1. Lagrangian particle tracking

Particle trajectory is determined upon time integration of the simplified Basset–Boussinesq–Oseen equation (Crowe et al., 1998). Modeling assumptions are: (i) particles are treated as non-interacting, non-deformable solid spheres; (ii) the average particle-to-fluid mass loading ratio is small enough to neglect turbulence modulation induced by the particles; (iii) particles are heavy and particle-to-fluid density ratio is large: hence, contribution of unsteady forces like virtual mass, pressure gradient, and Basset to particle motion can be neglected (Chung and Troutt, 1988). In addition, we did not include the lift force in the equation of particle motion. The ratio between lift force (written using Saffman formulation, see Saffman, 1965, 1968) and Stokes drag is $F_L/F_D\sim\mathcal{O}\left[d_p\left(\frac{1}{\nu}\frac{\partial u_z}{\partial r}\right)^{0.5}\right]$, with d_p the particle diameter: In our simulations, $F_L/F_D\sim\mathcal{O}(10^{-3})$. Gravity was also not included since most of the practical instances of axial separators are found in vertical set-up, where gravity plays a negligible role in particle collection at the wall. Even if the horizontal configuration is possible, a computation for the present choice of parameters gives a gravitational settling time $\tau_g=R/v_s$, with $v_s=g\tau_p$ the particle settling velocity in still fluid and $\tau_p=\rho_p d_p^2/18\mu$ the particle response time to turbulent fluctuations ($\rho_p=10^3$ kg/m^3 is particle density and μ is fluid dynamic viscosity), about one order of magnitude larger than the

centrifugal settling time, $\tau_c = R/v_c$, where the characteristic velocity $v_c = \tau_p(\Omega^2 R_c^2/R)$ can be obtained from a simple balance of drag force and centrifugal force in the radial direction. In particular, we find $\tau_g/\tau_c \simeq 5$ (resp. $\tau_g/\tau_c \simeq 20$) in the S_L (resp. S_H) simulation. The resulting governing equations for particle motion read as:

$$\frac{d^2\mathbf{x}_p}{dt^2} = \frac{d^2\mathbf{v}_p}{dt} = \mathbf{f}, \tag{5}$$

where $\mathbf{x}_p$ represents particle position in the (r,θ,z) space, $\mathbf{v}_p = (v_\theta, -v_r, v_z)$ is particle velocity and $\mathbf{f}$ is the total force per unit mass exerted by the fluid on the particle. The corresponding set of scalar differential equations is:

$$\begin{cases} r\frac{d^2\theta}{dt^2} = \frac{dv_\theta}{dt} = \frac{C_d}{\tau_p}(u_{\theta,p} - v_\theta) - \frac{v_\theta v_r}{r} \\ \frac{d^2r}{dt^2} = \frac{dv_r}{dt} = \frac{C_d}{\tau_p}(u_{r,p} - v_r) + \frac{v_\theta^2}{r} \\ \frac{d^2z}{dt^2} = \frac{dv_z}{dt} = \frac{C_d}{\tau_p}(u_{z,p} - v_z) \end{cases} \tag{6}$$

where $u_{\theta,p}$, $u_{r,p}$ and $u_{z,p}$ are the fluid velocity components at the particle location obtained using a tri-linear interpolation scheme in cylindrical coordinates (Marchioli et al., 2003; Sbrizzai et al., 2009); $C_d = 24Re_p^{-1}(1 + 0.15Re_p^{0.687})$ is the non-linear drag coefficient (Schiller and Naumann, 1935), with $Re_p = |u_{i,p} - v_i|d_p/\nu$ the particle Reynolds number. The same numerical methodology has been recently used by Bernardini et al. (2013) to study particle dispersion in Poiseuille and Couette turbulent channel flow.

Due to pipe geometry, the system of Eq. (6) has a singularity associated with the solution at the pipe centerline. To circumvent the problem, equations are written in transformed variables, following a procedure similar to that adopted for the fluid governing equations. In particular, the independent variable $Q_\theta = r \cdot \theta$ was chosen as auxiliary coordinate for particle position in the azimuthal direction. The complete set of particle equations written using Q_θ is reported elsewhere (Marchioli et al., 2003; Sbrizzai et al., 2009). Particle equations are advanced in time using a fifth-order adaptive Runge–Kutta scheme and assuming a time piecewise constant velocity field of the gas phase, which was considered frozen within each time interval of the simulation. This approximation is justified by the fact that the timestep for particle tracking (which is the same as for the fluid) is much smaller than both the Kolmogorov timescale of fluctuations based on the volume-averaged viscous dissipation, τ_K, and the particle relaxation time ($\Delta t_{DNS} \simeq [10^{-2}\text{–}10^{-1}]\tau_p$, depending on particle diameter, see Marchioli et al., 2003). The total tracking time was $\Delta t/\mathcal{T} \simeq 10(\Delta t^+ \simeq 230)$, enough for all injected particles to cover the entire pipe length at least once. Particles were initially released in the entire pipe with random distribution in the (r,θ,z) domain to generate a numerical condition best suited for computing time-averaged statistics. Particle initial velocity was set equal to that of the fluid interpolated at the particle location. Particles exiting the outlet section were removed from the flow and re-injected at the inlet section upon re-initialization of position and velocity. Particle–wall interaction is modeled considering two opposite situations: perfectly elastic rebound for solid particles that come closer than one particle radius from the boundary, perfectly absorbing wall for liquid droplets.

Three different values of the particle Stokes number, $St = \tau_p/\tau_f$, were considered, for a total of 9 simulated cases in the (Re_τ, S, St) parameter space: $St \simeq 0.27$, 1.27 and 11.1, corresponding to $d_p = 10$, 25 and 65 μm, respectively. Here, $\tau_f = \nu/u_\tau^2$ is the viscous timescale, chosen as characteristic timescale of the fluid (Crowe et al., 1998). In our flow, $\tau_f \simeq 1.35 \times 10^{-3}$ s, smaller than the mean Kolmogorov timescale, $\tau_K \simeq 4.5 \times 10^{-3}$ s. Values of the particle Stokes number based on τ_K can be readily obtained as $St_K = St \cdot \tau_f/\tau_K \simeq St/3$. For each particle set, the total number of tracked particles is $N_p^{tot} = 10^5$.

Note that particle diameter (particle inertia) scales as Re^{-1} when St is kept constant: Hence, the behavior observed at $Re = 5000$ is expected to reproduce well the physics of particle/droplet separation at Reynolds numbers up to one order of magnitude higher.

3. Results and discussion

A specific feature of the present work is the swirling flow induced by a rotating fluid core rather than a rotating wall as in axially-rotating pipes (Steenbergen and Voskamp, 1998; van Esch and Kuerten, 2008; Orlandi and Fatica, 1997). For future benchmark we present a detailed statistical characterization of the flow field. This is complemented by a phenomenological analysis of particle trapping by swirl-modulated near-wall turbulence and by a quantitative evaluation of collection efficiency and deposition velocity.

3.1. Mean flow field

Fig. 3 shows the mean profiles of the axial fluid velocity, $\langle u_z \rangle$, of the azimuthal fluid velocity, $\langle u_\theta \rangle$, and of the axial fluid vorticity, $\langle \omega_z \rangle/N$ for all swirl intensities. Profiles are taken at different axial locations along the pipe, with quantities expressed in outer units and vorticity normalized by the rotation number. Note that, in the spatially-developing pipe flow, space-averaging can be performed only in the azimuthal direction. The mean axial velocity distribution in the S_H case (Fig. 3a, symbols) differs significantly from that obtained with zero swirl (S_0 case, solid line) at the same flowrate: swirl induces larger axial velocity, and in turn higher mean shear, in the near-wall region ($0.7 \leqslant r/R \leqslant 1$) but lower axial velocity in the central region ($r/R < 0.7$), where $\langle u_z \rangle$ develops a dip across the pipe centerline as a result of the concentrated-vortex swirl imposed at the pipe inlet. This velocity dip is advected downstream with a slow decay rate: it can still be observed at about 20 radii downstream of the inlet section. In the S_L case (Fig. 3b) the mean shear near the wall (resp. near the pipe centerline) is again higher (resp. lower) than without swirl but the spin initially imparted to the fluid is much weaker and the velocity dip vanishes within few diameters from the inlet. The azimuthal velocity, Fig. 3c–d, exhibits the expected structure consisting of a core region, an annular region and a wall region (Kitoh, 1991). The extent of each vortex region changes depending on the swirl intensity and transition from one region to another becomes less evident as swirl intensity decreases.

In the core region ($0 < r/R < 0.2$ for the S_H case, $0 < r/R < 0.3$ for the S_L case) the tangential velocity has a forced-vortex distribution ($v_\theta \propto r$) characterized by high angular velocity. A velocity profile of this type strongly stabilizes turbulence and the small flow scales should vanish rapidly. In the core region only large-scale motions are thus expected to survive over long distances downstream of the inlet section (Kitoh, 1991).

In the annular region ($0.2 < r/R < 0.9$ for the S_H case, $0.3 < r/R < 0.8$ for the S_L case) the tangential velocity has a free-vortex distribution ($v_\theta \propto 1/r$) with nearly constant angular momentum. As a consequence, swirl produces a local minimum of $\langle u_\theta \rangle$ for $0.6 < r/R < 0.8$. This minimum becomes less marked as the swirling motion approaches the outlet assuming a velocity distribution characteristic of solid body rotation (particularly in the S_L case).

In the wall region, the velocity gradient is quite steep and remains nearly constant along the axial direction. The observed behavior of fluid velocities agrees qualitatively with the experimental measurements of Kitoh (1991), and Steenbergen and Voskamp (1998), who considered non-rotating pipe flow with

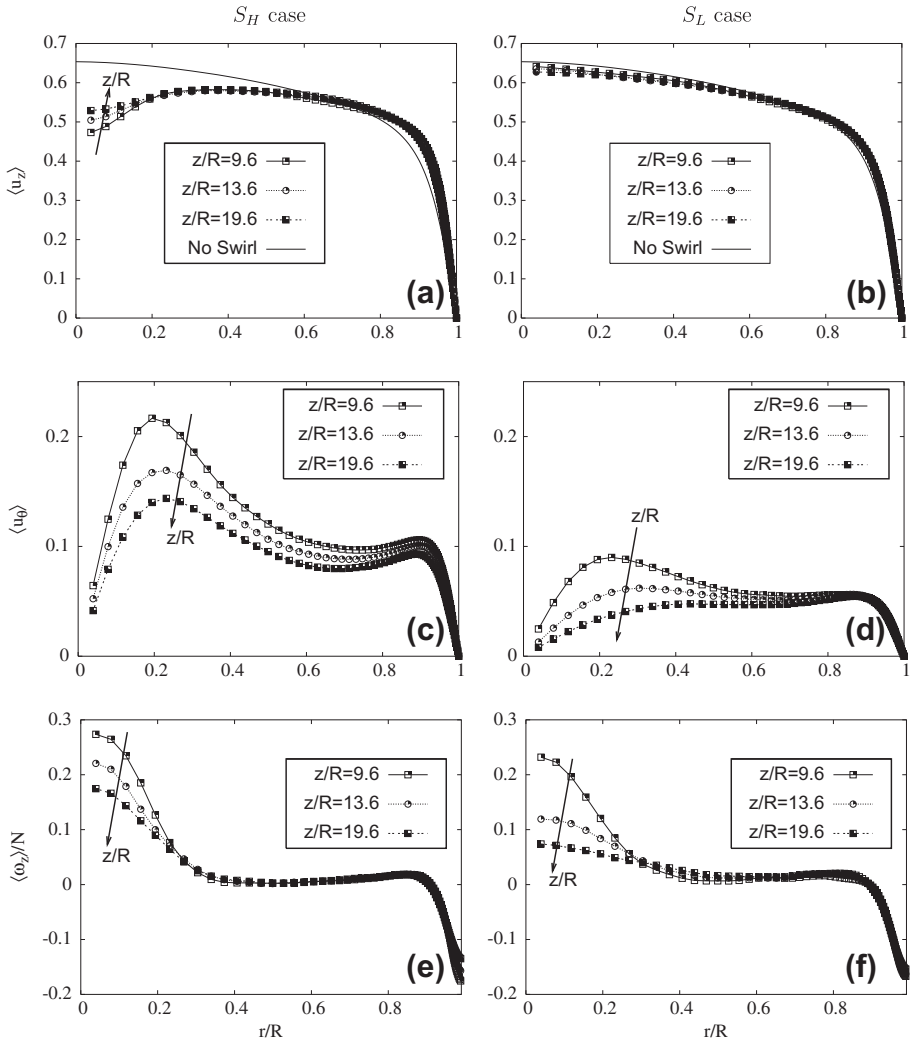

Fig. 3. Mean fluid velocity and vorticity in the spatially-developing swirled pipe flow for the S_H case (left-hand panels) and for the S_L case (right-hand panels). Panels: (a and b) axial velocity, $\langle u_z \rangle$; (c and d) azimuthal velocity, $\langle u_\theta \rangle$; (e and f) axial vorticity, $\langle \omega_z \rangle / N$. Quantities are in outer units. Profiles are taken at different axial locations downstream of the inlet section (z/R = 9.6, 13.6 and 19.6).

comparable values of the swirl number but much higher values of the bulk Reynolds number ($Re \geqslant 50{,}000$). The similarity among profiles at varying Re may suggest the existence of a scaling behavior of the mean flow field with respect to the swirl intensity. We notice no similarity with the fluid velocity profiles obtained in axially-rotating pipes where, opposite to what we find, the mean axial velocity approaches the laminar Poiseuille profile at increasing swirl intensities and the $\langle u_\theta \rangle$-profile has zero slope at the wall (Steenbergen and Voskamp, 1998; Kitoh, 1991; Orlandi and Fatica, 1997). Accordingly, the present cases have higher fluid velocity wall-gradients (and in turn higher wall shear stress) compared with rotating pipes.

The flow field characteristics can be also appreciated examining the mean axial vorticity, shown in Fig. 3e–f. The magnitude of axial vorticity is higher near the rotating fluid core and near the pipe wall, where the increase of $\langle \omega_z \rangle$ is due to secondary shearing motions associated with strong velocity gradients rather than to swirl-induced rotation. A change of sign occurs between these two regions, with an intermediate plateau ($0.4 < r/R < 0.8$) of nearly zero vorticity in the annular region where v_θ scales with $1/r$. Another feature shared by all $\langle \omega_z \rangle$ profiles regardless of swirl strength is a significant axial decay of vorticity near the pipe center, where the axial velocity dip occurs, and very close to the wall, where $\omega_z \simeq \partial u_\theta / \partial r$. The behavior of $\langle \omega_z \rangle$ just described resembles not at all that observed in rotating pipes (Orlandi, 2000).

A collective analysis of the statistics shown in Fig. 3 reveals that swirl onset and subsequent decay is linked to a change of the wall shear stress. To examine this change, in Fig. 4, we look at the tangential wall shear stress components:

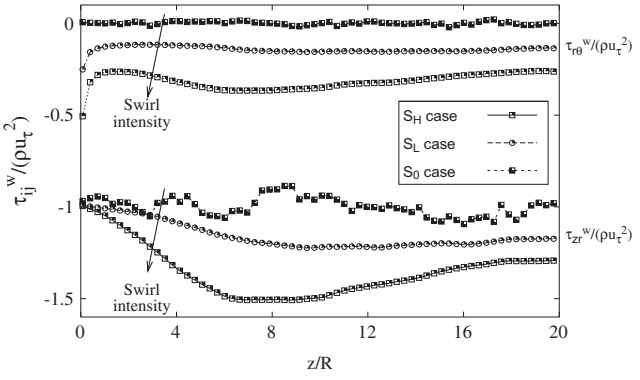

Fig. 4. Axial behavior of the normalized wall shear stress components, $\tau_{zr}^w/\rho u_\tau^2$ and $\tau_{r\theta}^w/\rho u_\tau^2$, for the different swirl intensities.

$$\frac{\tau_{rz}^w(z)}{\rho u_\tau^2} = \mu \frac{\partial u_z}{\partial r}\bigg|_{r=R} = -\mu\omega_\theta(z)^w,$$
$$\frac{\tau_{r\theta}^w(z)}{\rho u_\tau^2} = \mu\left[r\frac{\partial}{\partial r}\left(\frac{u_\theta}{r}\right)\right]\bigg|_{r=R} = \mu\omega_z(z)^w.$$

Note that both shear stresses are azimuthally averaged. Upon comparison of the different profiles at varying swirl strength, two main conclusions can be drawn. First, the swirl imparted to the fluid increases τ_{rz}^w with respect to the S_0 case: At a distance of about 20 pipe radii downstream of the inlet section, τ_{rz}^w increases by roughly 20% (resp. 35%) for the S_L (resp. S_H) case. Second, due to fluid rotation, the magnitude of $\tau_{r\theta}^w$ is significantly different from zero at all axial locations examined. Hence, this component of the stress tensor becomes important in the Reynolds stress transport equation (Kitoh, 1991). The swirl-induced wall shear stress modification is accompanied by a change of both axial and azimuthal friction velocities, $u_{\tau z}(z) = \sqrt{\tau_{rz}^w(z)/\rho}$ and $u_{\tau\theta}(z) = \sqrt{\tau_{r\theta}^w(z)/\rho}$. Fig. 4 shows that these two velocities increase proportionally to the swirl intensity. Accordingly, the axial and azimuthal Reynolds numbers, defined as $Re_{\tau z}(z) = u_{\tau z}(z)R/\nu$ and $Re_{\tau\theta}(z) = u_{\tau\theta}(z)R/\nu$ respectively, attain values larger than Re_τ in the S_0 case, as shown in Table 1. Note that $u_\tau = u_{\tau z}|_{S=0}$ (with $u_{\tau\theta}|_{S=0} = 0$) and $Re_\tau = Re_{\tau z}|_{S=0}$ (with $Re_{\tau\theta}(z)|_{S=0} = 0$) since the shear velocity is derived from a force balance in the axial direction.

The above observations suggest that the mean fluid velocity profiles shown in Fig. 3a–b can be examined objectively upon renormalization based on the shear velocity instead of U_{cP}. By doing so, profiles are expressed in wall units and provide interesting information about swirl-induced drag modifications which cannot be obtained from Fig. 3a–b. In Fig. 5, we show the dimensionless axial fluid velocity $\langle u_z^+(r,z)\rangle = \langle u_z(r,z)/u_{\tau z}(z)\rangle$ for the S_L case (Fig. 5a) and for the S_H case (Fig. 5b), respectively. Compared to the S_0 case (solid line), swirl-flow rescaled profiles (symbols) overlap almost perfectly in the near-wall region (up to $r^+ = (R-r)u_{\tau z}/\nu \simeq 10$) and effects due to swirl are negligible. Farther away from the wall ($r^+ > 10$), swirl-flow profiles always attain lower values than in the S_0 case with significant axial decay only in the S_H case (Fig. 5b). This behavior indicates that if the pressure gradient driving the flow is imposed (namely the wall shear stress is "kept" constant) then swirl reduces the flowrate. This phenomenon is a macroscopic manifestation of swirl-induced drag enhancement. Opposite drag modifications are observed in rotating pipes, where a clear tendency towards re-laminarization of turbulence is observed at increasing swirl numbers (Orlandi and Fatica, 1997; Kitoh, 1991; Eggels, 1994; Nygard and Andersson, 2010).

3.2. Swirl number and intensity decay rates

In wall-bounded swirling flows, tangential fluid motions decay downstream at a rate that can be measured as (Kitoh, 1991; Parchen and Steenbergen, 1998):

$$S(z) = \frac{\dot{G}_\theta(z)}{R\dot{G}_z(z)} = \frac{2\pi\rho\int_0^R\langle u_z(r,z)\rangle\langle u_\theta(r,z)\rangle r^2 dr}{\rho\pi R^3 U_b^2}, \quad (7)$$

where $\dot{G}_\theta(z)$ is the axial flux of angular momentum, and $\dot{G}_z(z)$ is the axial flux of axial momentum. The axial evolution of S characterizes the decay process (Kitoh, 1991). Previous studies (Kitoh, 1991; Parchen and Steenbergen, 1998) have shown that, for the swirl intensities and the swirl type considered in this study, the decay rate is best fitted by an exponential law:

$$S(z) = S_r \cdot \exp\left[-\beta\left(\frac{z_r - z}{D}\right)\right], \quad (8)$$

where $S_r = S(z_r)$ is the swirl intensity at a suitably-selected reference location z_r and β is the Re-dependent decay coefficient. As indicated by Kitoh (1991), the exponential decay is obtained only if $\tau_{r\theta}^w \propto S$, hence Eq. (8) is not accurate for very high swirl numbers ($S \gg 0.2$). Fig. 6 shows the axial behavior of S for the S_H case (symbols), and the decay rate predicted by Eq. (8), which is found to best-fit numerical results using $\beta = 0.0262$ (solid line). For comparison purposes, present numerical results are plotted together with the exponential fit proposed by Kitoh (1991). Note that only the second half of the domain ($z/R \geqslant 10$) is considered because the initial stage of the decay exhibits deviations from the exponential fit (Steenbergen and Voskamp, 1998): in the selected portion of the domain, the swirl intensity S is thus normalized using $S_r = S(z_r = 10R)$. As expected, our profiles are below the experimental fits due to the smaller Reynolds number but follow the exponential decay rather well. Results for the S_L case (not shown for brevity) are qualitatively similar and yield best exponential fit for $S_L = 0.085$ with $\beta = 0.023$: this confirms that the swirl decay rate decreases for increasing S within the range of swirl intensities considered in this study (Steenbergen and Voskamp, 1998).

Table 1
Bulk and shear Reynolds numbers in the spatially-developing swirled pipe flow for the different swirl intensities. Reference values of $Re_{\tau z}$ and $Re_{\tau\theta}$ are taken at $z/R = 19.6$ downstream of the inlet section.

Reynolds number	S_0 case ($S_0 = 0, N = 0$)	S_L case ($S_L = 0.085, N = 0.5$)	S_H case ($S_L = 0.17, N = 1$)
$Re = U_{cP}R/\nu$	5000	5000	5000
$Re_{\tau z} = u_{\tau z}R/\nu$	171	187	198
$Re_{\tau\theta} = u_{\tau\theta}R/\nu$	0	62	86

3.3. Swirl effects on particle preferential concentration and wall accumulation

There is experimental (Balachandar and Eaton, 2010) and numerical (Marchioli and Soldati, 2002; Soldati and Marchioli, 2009) evidence that heavy particles in confined swirl-free turbulent flow exhibit non-uniform spatial distribution. The degree of non-uniformity strongly depends on particle inertia and is induced by particles-turbulence interaction at the particle scale: driven by turbulence, particles are known to segregate into clusters, migrate towards the wall (turbophoretic drift, see Reeks, 1983), and, when in the wall layer, concentrate preferentially within low-speed streaks (Marchioli and Soldati, 2002). Near-wall accumulation is typically observed over a long time transient characterized by unbalanced particle transfer fluxes to and off the wall (Picciotto et al., 2005; Zhao et al., 2012; Zonta et al., 2011). After this transient, very few particles are left in the outer flow region and transfer fluxes finally balance each other (Marchioli et al., 2008b). Particle transport to/off the wall is driven by in-sweeps of high momentum fluid towards the wall and ejections of low-momentum fluid away from the wall (Marchioli and Soldati, 2002; Zonta et al., 2008). Fluid streaks are the instantaneous footprint of these events. Aim of this section is to examine the persistence of turbulence-induced trapping mechanisms (segregation into streaks, in particular) when particles experience both turbophoretic drift and centrifugal motion.

Fig. 7 shows cross-sectional views of particle instantaneous distribution and corresponding contour map of the axial fluid vorticity, ω_z: regions of high positive (resp. negative) vorticity are visualized in white (resp. black). To highlight the axial dependency of particles and fluid behavior, two different $r-\theta$ sections have been selected: $z/R = 9.6$ (top panels) and $z/R = 13.6$ (bottom panels). In addition, all particle sets have been considered to discuss how inertial effects can modulate particle response to swirl-induced centrifugation. For ease of discussion, only results relative to the last simulated time step ($t^+ \simeq 230$) in the S_H case are shown. The effect of rotation on particle dynamics and the

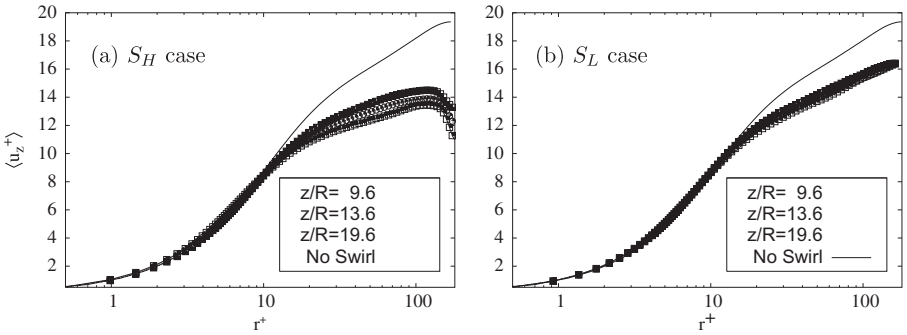

Fig. 5. Rescaled mean fluid axial velocity, $\langle u_z^+(r,z)\rangle = \langle u_z(r,z)/u_{\tau z}(z)\rangle$, in the spatially-developing swirled pipe flow. Panels: (a) S_H case, (b) S_L case. Note that $r^+ = (R-r)\cdot u_{\tau z}/\nu$.

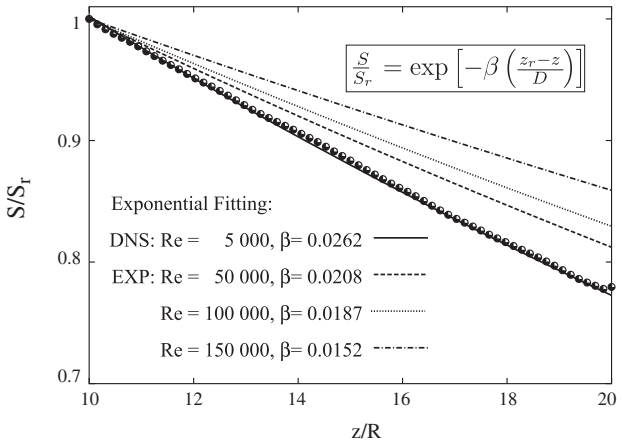

Fig. 6. Axial decay of normalized swirl intensity, S/S_r, in the range $10 < z/R < 20$ for the S_H case. Symbols: DNS data; solid line: fit of DNS data with $\beta = 0.0262$ in Eq. (8); dashed/dotted lines: fit of experimental data of Kitoh (1991) with $\beta = 0.0208$, 0.0187 and 0.0152 in Eq. (8) for $Re = 5\times10^4$,10^5 and 1.5×10^5, respectively.

non-random fashion of particle distribution are evident, especially for the larger, more inertial particles (see Fig. 7a and d for the $St = 11.1$ particles; Fig. 7b and e for the $St = 1.7$ particles). Similarly to what happens in swirl-free flows, particles with high-enough inertia are flung out of vortices and tend to cluster at the vortex periphery, in regions of low vorticity and high strain rate (gray areas). This is evident in the core region of the pipe, where large-scale vortices form due to the forced-vortex swirling motion and produce regions depleted of particles. Void regions are also found near the wall, where the turbulent structures responsible for the turbophoretic drift of particles are located. The selective response of particles to the underlying swirled turbulence is also apparent. The large $St = 11.1$ particles, for which $\tau_p/\tau_c \simeq O(1)$, can easily cut across vortices under the effect of the centrifugal force and are propelled towards the pipe wall; The small $St = 0.27$ particles have $\tau_p/\tau_c \simeq O(10^{-3})$ and, therefore, are little influenced by centrifugation: their dynamics will follow almost exactly that of near-wall turbulent structures. As expected, the $St = 1.7$ particles ($\tau_p/\tau_c \simeq O(10^{-2})$) exhibit an intermediate behavior.

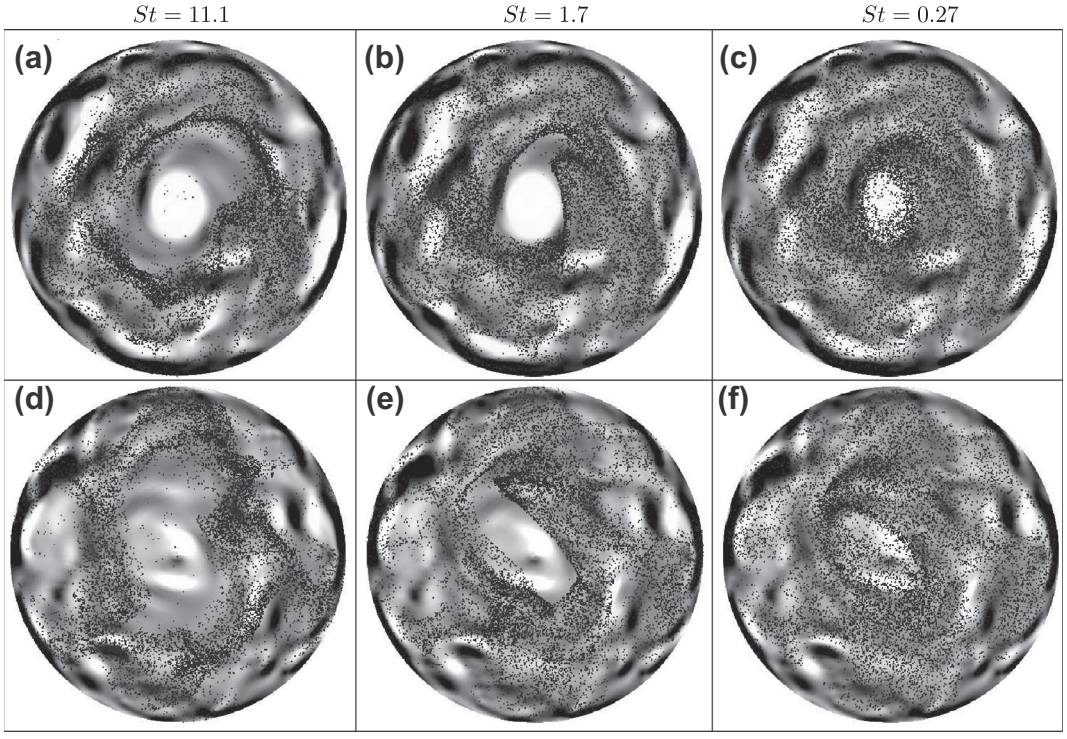

Fig. 7. Instantaneous distribution of axial fluid vorticity (ω_z) and of particles at two different axial locations ($z/R = 9.6$, top panels; $z/R = 13.6$, bottom panels) in the spatially-developing swirled pipe flow (S_H case). Black and white colors indicate negative and positive vorticity, respectively. Panels: (a), (d) $St = 11.1$; (b), (e) $St = 1.7$; (c), (f) $St = 0.27$.

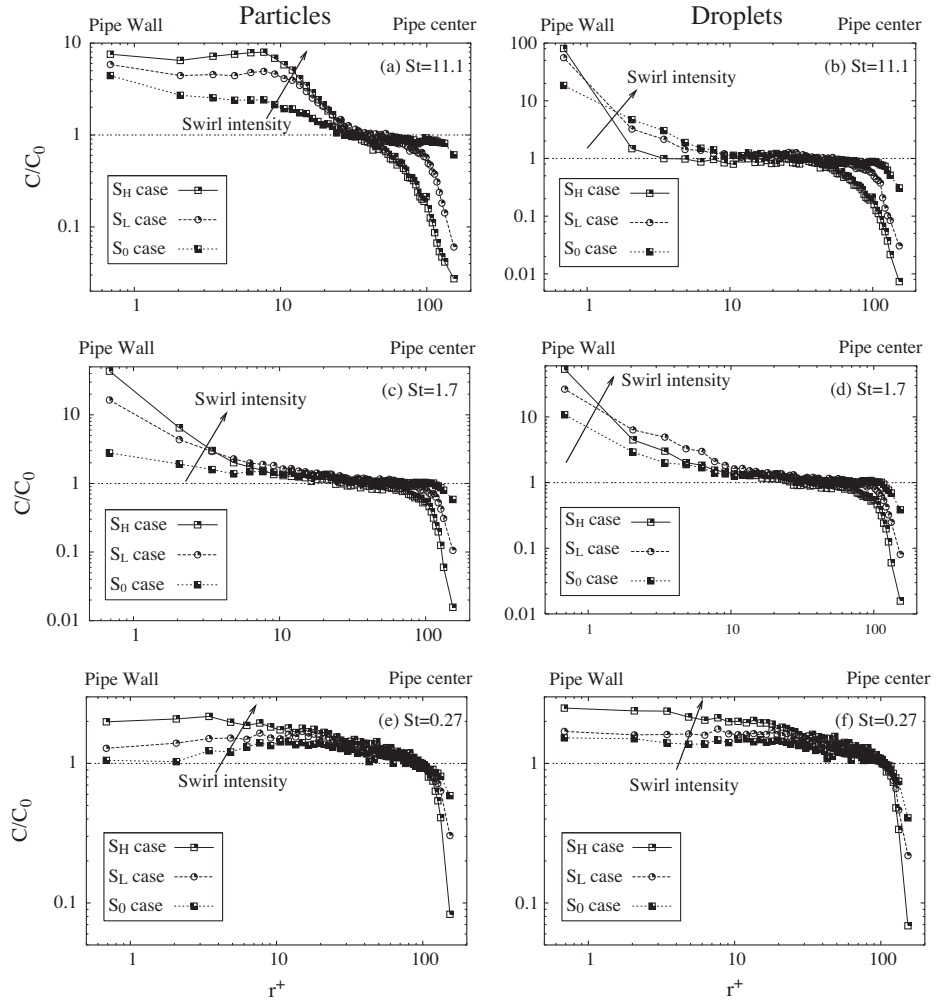

Fig. 8. Particles and droplets concentration along the pipe radius at varying swirl intensity. Panels: (a), (b) $St = 11.1$; (c), (d) $St = 1.7$; (e), (f) $St = 0.27$. Left-hand-side panels: particles; right-hand-side panels: droplets.

Regardless of their size, however, all particles eventually accumulate at the wall, producing peaks of concentration inside the viscous sublayer. Fig. 7 alone is not sufficient to show any statistical effect resulting from preferential concentration. To verify whether such effect exists in a mean sense, in Fig. 8 we compare particle and droplet concentration profiles with and without swirl, at varying particle inertia as a function of the non-dimensional distance from the pipe wall, r^+. All swirl intensities and all particle/droplet sets are considered. Concentration profiles represent the number density of particles and droplets along the radial coordinate at time $t^+ = 230$, obtained subdividing the computational domain into $N_s = 62$ slabs of equal volume $V_s = \pi L(r_s^2 - r_{s-1}^2)$ along the radial coordinate (with $r_0 = 0$ and $r_{N_s} = R$) and counting at the chosen time step t the number $N_p(s,t)$ of particles within each slab s. Concentration is then computed as $C(s,t) = N_p(s,t)/V_s$ with $C_0 = C(s, t = 0)$ corresponding to the initial particle distribution.

From Fig. 8a, c and e we can observe that particles in the S_0 case generate a peak of concentration in the near-wall region (Marchioli et al., 2003). Particle inertia determines the shape of the profile and the location of the peak, which occurs right at the wall for the larger particles (last point on the left end of each curve) and within the buffer layer for the smaller particles (at $r^+ \simeq 20$ for the $St = 0.27$ particles in the present simulations). As expected, Fig. 8a, c and e shows that, for all particle sets examined, swirl increases near-wall concentration while depleting the pipe core with respect to the S_0 case. The highest increase is observed for the $St = 1.7$ particles, which are characterized by a peak concentration value in the S_H case about 20 times larger than in the S_0 case. A closer examination of Fig. 8a, which refers to the $St = 11.1$ particles, reveals that a second concentration peak may develop away from the wall as the swirl intensity increases. In both S_L and S_H cases, such peak is located at $r^+ \simeq 8$. This behavior can be explained considering that particles bounce elastically off the wall, keeping the kinetic energy and momentum possessed at impact. For the larger particles, the wallward drift generated by the combined effect of turbophoresis and swirl-induced centrifugation is high enough to permit re-entrainment in the outer region once "converted" in outward drift after rebound. A further accumulation layer then develops around the radial location at which outward and wallward drifts balance again. In Fig. 8b, d and f we show the concentration profiles for droplets. It can be readily seen that concentration always peaks at the wall (no elastic rebound effect) and that profiles cross-over farther away from the wall as droplet inertia decreases, indicating a reduced effect of centrifugal drift (compared to turbophoretic drift) at smaller St.

In swirl-free flows, non-uniformities in the radial direction due to intermittent concentration are accompanied by non-uniformities in the azimuthal wall-parallel direction when inertial particles are segregated in the wall region (Marchioli and Soldati, 2002; Marchioli et al., 2003). This feature is observed also in the present

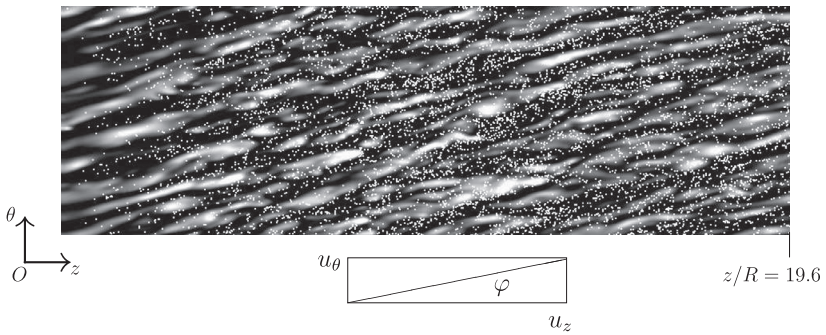

Fig. 9. Instantaneous distribution of $St = 11.1$ particles and high/low-speed fluid streaks in the spatially-developing swirled pipe flow. Visualization refers to the $\theta - z$ plane at $r/R = 0.8$ in the S_H case. Black and white colors indicate negative and positive fluctuations, respectively. The mean inclination of the swirl angle φ, representing the tilting of the fluid velocity vector in the $\theta - z$ plane, is also shown.

simulations with swirl as demonstrated, for instance, in Fig. 9. In this figure the instantaneous distribution of the $St = 11.1$ particles on a wall-parallel $\theta - z$ plane at $r/R = 0.8$ in the S_H case is superimposed to the instantaneous axial velocity fluctuations of the fluid, u'_z. Streaks clearly appear tilted with an inclination angle corresponding to the swirl angle $\varphi = \arctan(u_\theta/u_z)$ (Nygard and Andersson, 2010). The correlation between particle location and low-speed streaks is evident: particles tend to line up along the streaks avoiding high-speed regions. Clearly, particle streaks exhibit the same tilting as fluid streaks, corroborating the conclusion that the coherent swirling motion does not disrupt the near-wall structures responsible for preferential concentration, wall accumulation and trapping. To quantify the tendency of particles to segregate into streaks, in Fig. 10 we show the Probability Distribution Function (PDF), $P(u_z'^+)$ computed at particle position in the wall region ($3 < R^+ - r^+ < 10$). In particular, we compare the PDF for swirl-free flow (Fig. 10c) with those obtained for swirled flow: S_L case in Fig. 10b), S_H case in Fig. 10a). Curves in each panel correspond to the different particle diameters. Confirming the qualitative observations drawn from Fig. 9, PDFs always peak at negative values of $u_z'^+$. Compared to the swirl-free flow, however, the magnitude of the peak is higher in presence of swirl. Maximum values are observed for the S_L case, with a slight reduction for the S_H case (probably an effect due to elastic particle collision against the wall). Also the shape of $P(u_z'^+)$ appears more sensitive to changes of particle size in swirled flow: Peaks shift towards more negative values of $u_z'^+$ for the two larger particle sets ($St = 1.7$ and $St = 11.1$) as swirl intensity increases. The observed behavior indicates that, within the investigated range of swirl numbers ($S < 0.2$), swirling motions favor particle segregation into streaks provided that particle inertia is sufficiently high ($St \geqslant 1$ in the present simulations), and their mutual interaction with near-wall structures is beneficial for separation purposes. The PDF for the smaller particles ($St = 0.27$) is less skewed towards negative values of $u_z'^+$ and is less affected by a change of swirl strength. This behavior is due to the low inertia of these particles, which behave almost like fluid tracers and exhibit a more persistent stability against non-homogeneous distribution and near-wall concentration.

3.4. Separation of particles

In this subsection we examine the separation process of inertial particles, for which elastic rebound conditions are considered. Deposition rates and collection efficiencies can be evaluated determining the net mass of particles that can be separated along the axial direction when both particle inertia and swirl strength vary. To compute this quantity, we considered a reference annular region of thickness $\Delta r^{sep} = R - r^{sep}$ near the wall and counted the number of particles, $N_p^{sep}(t)$, within this region at a given time instant t of the simulation. When the residence time of a particle trapped inside the annular region is large enough (larger than a suitably-chosen threshold value), then that particle is considered as separated from the gas stream and collected at the wall. We computed the threshold residence time as $T_{res} = \Delta r^{sep}/v_{dep}$, corresponding to the time taken by particles to cross the near-wall collection region entering at radial coordinate r^{sep} with velocity $v_{dep}(r = r^{sep}) = \tau_p \frac{u_\theta^2(r=R_c)}{r^{sep}} \simeq \tau_p \left[\frac{\Omega^2 R_c^2}{r^{sep}}\right]$. Fig. 11 compares the axial evolution of $N_p^{sep}(t)$, normalized by the total number of injected particles N_p^{tot}, at the final timestep of the simulations with swirl (solid line: S_H case; dotted line: S_L case) and of the swirl-free simulation (dash-dotted lines: S_0 case). Note that $z/R \simeq t \cdot U_b/\mathcal{T}$. Results are shown for two different values of Δr^{sep}: $\Delta r^{sep}/R = 0.1$ and 0.04, corresponding to separation volumes $V^{sep} = \pi L[R^2 - (r^{sep})^2]$ equal to 19% and 8% of the total pipe volume, respectively. The cross section for the different separation volumes is visualized with insets in each panel of Fig. 11 and highlighted in black. The range of thresh-

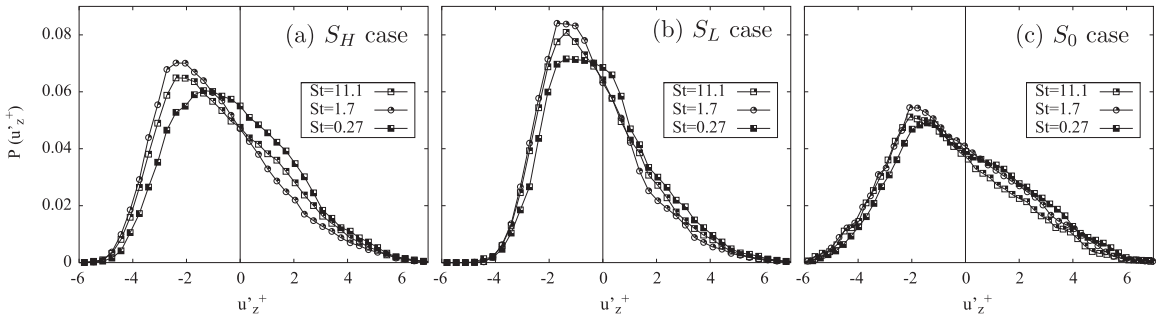

Fig. 10. Probability distribution function, $P(u_z'^+)$, of fluctuating streamwise velocity, $u_z'^+$, computed at particle position in the wall region ($3 < R^+ - r^+ < 10$) for varying swirl intensity. Panels: (a) S_H case; (b) S_L case; (c) S_0 case.

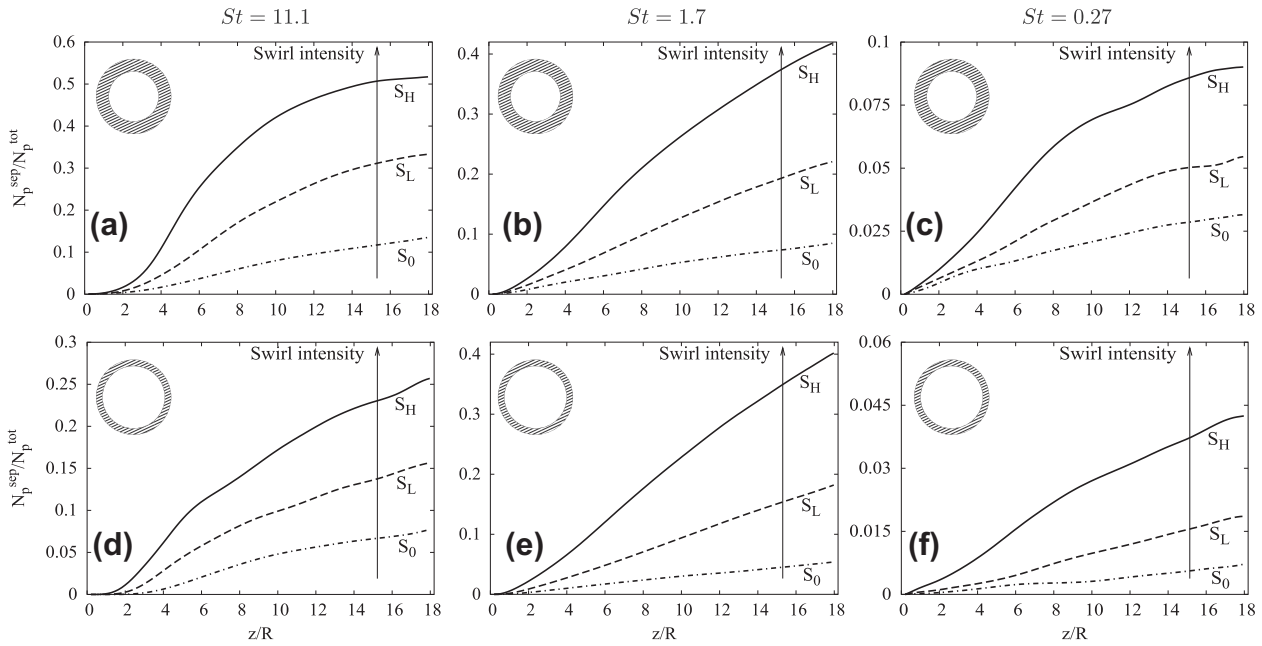

Fig. 11. Number of separated particles along the axial direction in the spatially-developing swirled pipe flow. Particles are considered as separated if their residence time within the annular near-wall region highlighted in the inset of each panel is higher than the threshold value T_{res} defined in Section 3.4. Columns: (a) and (d) St = 11.1; (b) and (e) St = 1.7; (c) and (f) St = 0.27; Rows: (a–c) $\Delta r^{sep}/R$ = 0.1 (V^{sep}/V_{tot} = 19%); (d–f) $\Delta r^{sep}/R$ = 0.04 (V^{sep}/V_{tot} = 8%).

old residence times is, in wall units, $0.89 < T^{+}_{res} < 158$ for the S_L case and $0.22 < T^{+}_{res} < 39.5$ for the S_H case.

Comparison among the different cases shows the impact of swirl on the collection efficiency, especially for the larger particles. The increase in the number of particles that can be separated along the pipe axis is evident: for the St = 11.1 particles and a reference separation volume $V^{sep}/V_{tot} \simeq 19\%$ (Fig. 11a), we find $N_p^{sep}/N_p^{tot} \simeq 0.52$ (resp. $N_p^{sep}/N_p^{tot} \simeq 0.33$) in the S_H case (resp. S_L case) near the streamwise end of the separator ($z/R \simeq 18$): Compared to $N_p^{sep}/N_p^{tot} \simeq 0.13$ in the S_0 case, this yields a +300% (resp. +153%) increase of separation, respectively. The increase is remarkable also for the intermediate-size particles, for which we find $N_p^{sep}/N_p^{tot} \simeq 0.42$ (resp. $N_p^{sep}/N_p^{tot} \simeq 0.22$) in the S_H case (resp. S_L case), compared to $N_p^{sep}/N_p^{tot} \simeq 0.09$ in the S_0 case. In agreement with the results previously discussed, the trend is less marked for the smaller particles, for which we find a +200% increase of separation even when a significant swirling motion is applied ($N_p^{sep}/N_p^{tot} \simeq 0.09$ in the S_H case, $N_p^{sep}/N_p^{tot} \simeq 0.03$ in the S_0 case). Not surprisingly, the increase of N_p^{sep}/N_p^{tot} within this separation layer is proportional to the increase of particle inertia at fixed swirl strength. Particle separation follows a less straightforward evolution when $V^{sep}/V_{tot} \simeq 8\%$. In this case, after an initial transient section comprised between the inlet pipe section and $z/R \simeq 6$ (resp. $z/R \simeq 12$) for the S_H case (resp. S_L case), the St = 1.7 particles separate better than the St = 11.1 particles, especially in the S_H case where more energetic rebounds are expected. This is again due to the elastic rebound boundary condition, which facilitates the formation of outward fluxes upon wall impact as particle inertia increases. From a modeling perspective, it is interesting to observe that present DNS results confirm the phenomenological model proposed by Chibbaro and Minier (2008) in the context of Langevin PDF simulations of turbulent particle deposition. The model is based on the notion of residence time and can be used to interpret present results since it assumes a rapid decrease of the residence time with particle diameter (according to the relation $dT_{res}/dd_p \propto -T_{res}$): as a consequence, deposition of high-inertia particles is very likely to occur each time they reach the wall, whereas deposition of low-inertia particles occurs at longer time scales.

3.5. Droplet separation and deposition velocity

In this section we examine the separation efficiency of droplets, for which an absorbing wall condition is considered. To this aim, in Fig. 12 we show the axial behavior of N_p^{sep}/N_p^{tot}. It can be readily

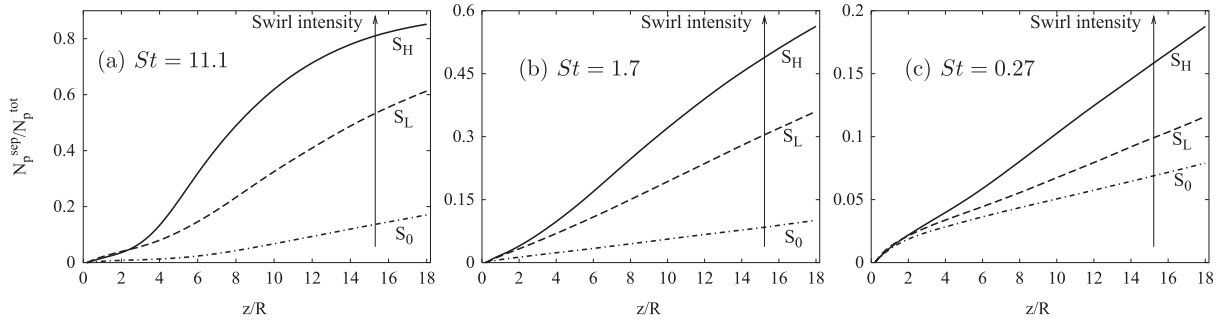

Fig. 12. Number of separated particles along the axial direction in the spatially-developing swirled pipe flow for the case of perfectly absorbing walls. Panels: (a) St = 11.1; (b) St = 1.7; (c) St = 0.27.

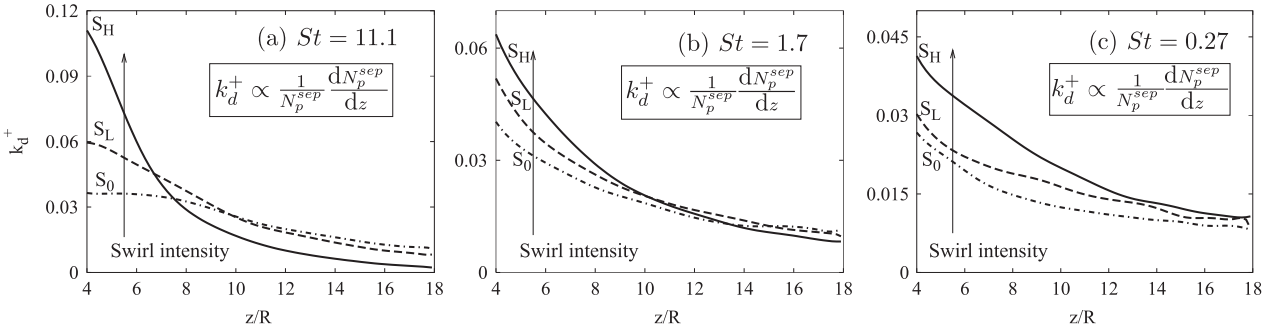

Fig. 13. Axial evolution of the non-dimensional particle deposition velocity, k_d^+, in the spatially-developing swirled pipe flow for the case of perfectly absorbing walls. Panels: (a) $St = 11.1$; (b) $St = 1.7$; (c) $St = 0.27$.

seen that separation is always proportional to swirl intensity regardless of droplet inertia. Values reached by N_p^{sep}/N_p^{tot} just before the outlet section of the separator are always higher than those measured in Fig. 11. This because no collection region was considered in the case of perfectly absorbing walls.

The rate of change in the number of separated droplets corresponds to their deposition velocity, defined as (Cousins and Hewitt, 1968):

$$k_d = \frac{J}{C} = \frac{U_{cP} \cdot r^{sep}}{2(z_2 - z_1)} \ln \frac{N_{p,1}^{sep}}{N_{p,2}^{sep}}, \tag{9}$$

where $J = U_{cP} \frac{dN_p}{dz} \frac{1}{A_{sep}}$ is the flux of droplets across the separation surface of area $A_{sep} \simeq 2\ \pi r^{sep} L$ and $C = N_p/V_{tot}$ is the bulk concentration outside the separation region, with $V_{tot} \simeq \pi (r^{sep})^2 L$ the pipe volume. Subscripts 1 and 2 in Eq. (9) represent two subsequent sampling stations along the pipe axis. The non-dimensional deposition velocity at varying swirl intensities is shown in Fig. 13. Profiles in this figure are plotted only for axial locations $z/R \geqslant 4$. This because we considered only those droplets initially released within a core-flow region comprised between the pipe axis and a given radial coordinate r^{sep}. The shortest axial distance covered by droplets while traveling wallward can be estimated for the largest droplets ($St = 11.1$ in the $S = S_H$ case with $r^{sep} = 0.8R$):

$$z/R = \frac{\Delta r^{sep}}{v_{dep}} \cdot \frac{U_b}{R} = \frac{(R - r^{sep}) r^{sep}}{\tau_p (\Omega \cdot R_c)^2} \cdot \frac{U_b}{R} \simeq 4. \tag{10}$$

In the initial part of the domain examined, for given droplet inertia, deposition velocity increases with swirl intensity. Well downstream of the separator a cross-over among k_d^+ profiles is observed for the larger droplets ($St = 11.1$, Fig. 13a; and $St = 1.7$, Fig. 13b). No cross-over is observed with the smaller droplets, for which k_d^+ increases with S ($St = 0.27$, Fig. 13c). This indicates that the deposition velocity of high-inertia droplets depends primarily on the term dN_p^{sep}/dz, which decreases monotonically with S along z/R, rather than $1/N_p^{sep}$, which increases monotonically with S along z/R. Eventually, all profiles relax toward the asymptotic value obtained for pipe flow (S_0 case).

4. Conclusions

In this work turbulence and particle dynamics in swirled pipe flow are investigated. The dispersed phase consists of a large number of micrometer-size particles with density much larger than that of the fluid (to simulate the dispersion of dust particles, droplets or aerosols in a gas stream). This flow configuration mimics the behavior of an axial swirl tube, a device found in several separation technology applications. The dynamics of the particle–fluid system is complex and is characterized by a wide range of mutually-interacting length and time scales (including those forced by the superimposed swirl) that contribute to particle dispersion. Direct numerical simulation and Lagrangian particle tracking are used to examine the effect of swirl on near-wall turbulence and to investigate the physical mechanisms that control particle separation.

Statistical and phenomenological analyses of the flow field indicate that, opposite to the case of swirl motions induced by wall rotation, a degree of drag increase is achieved due to higher velocity wall-gradients and a transport of axial vorticity toward the radial periphery of the pipe. Such modifications lead to an increase of wall shear stress and drag enhancement, which we have taken into account by rescaling dimensionless fluid velocity statistics based on a modified swirl-dependent axial friction velocity. This result is important in particle separation applications since it is known that turbulence wall transport mechanisms favor particle accumulation at the wall and, most importantly, trapping (Marchioli and Soldati, 2002; Soldati and Marchioli, 2009).

Further Lagrangian simulations have been used to verify particle wall transport efficiency in connection with turbulence modification. Within the examined range of swirl intensities, the superposition of a centrifugal swirling motion to the base flow does not disrupt the turbulent structures which control wall accumulation: statistics indicate that all macroscopic manifestations of particles/droplets interaction with turbulence in non-swirled flows do persist, proving that swirl may be exploited in combination with turbophoretic drift to increase collection efficiency and create optimal conditions for gas cleaning. In particular, we still observe trapping in the low-speed streaks and accumulation in the viscous sublayer. Transfer fluxes of particles and droplets along the axis of the separator are in agreement with the phenomenological model proposed by Chibbaro and Minier (2008). This model is based on the notion of residence time in the near-wall region and seems to be a good candidate for predicting deposition in swirled tubes.

Acknowledgments

Support from PRIN (under Grant 2006098584_004), from COST Action MP0806 and from HPC Europa Transnational Access Program (under Grants 466 and 708) is kindly acknowledged. This work was partially funded by the Italian Ministry of Productive Activities (under Grant MAP-ICE-CRUI, Project N. 99/2001), which is also gratefully acknowledged. Thanks to Professor Paolo Orlandi and to Professor Roberto Verzicco for having provided the flow solver.

References

Balachandar, S., Eaton, J.K., 2010. Turbulent dispersed multiphase flow. Annu. Rev. Fluid Mech. 42, 111–133.

Bernardini, M., Pirozzoli, S., Orlandi, P., 2013. The effect of large-scale turbulent structures on particle dispersion in wall-bounded flows. Int. J. Multiphase Flow 51, 55–64.

Bianco, F., Chibbaro, S., Marchioli, C., Salvetti, M.V., Soldati, A., 2012. Intrinsic filtering errors of Lagrangian particle tracking in LES flow fields. Phys. Fluids 24, 045103-1.
Chibbaro, S., Minier, J.-P., 2008. Langevin PDF simulation of particle deposition in a turbulent pipe flow. J. Aerosol Sci. 39, 555–571.
Chung, J.N., Troutt, T.R., 1988. Simulation of particle dispersion in a axisymmetric jet. J. Fluid Mech. 186, 199–222.
Cousins, L.B., Hewitt, G.F., 1968. Liquid Phase Mass Transfer in Annular Two-Phase Flow. UKAEA Report. AERE-R 5657.
Crowe, C., Sommerfeld, M., Tsuji, Y., 1998. Multiphase Flows with Droplets and Particles. CRC Press, New York.
Delfos, R., Murphy, S., Stanbridge, D., Olujic, Z., Jansens, P.J., 2004. A design tool for optimising axial liquid–liquid hydrocyclones. Min. Eng. 17, 721–731.
Eggels, J.G.M., 1994. Ph.D. Thesis. Delft University of Technology, The Netherlands.
Eggels, J.G.M., Unger, F., Weiss, M.H., Westerweel, J., Adrian, R.J., Friedrich, R., Nieuwstadt, F.T.M., 1994. Fully developed turbulent pipe flow: a comparison between direct numerical simulation and experiment. J. Fluid Mech. 286, 175–209.
Fukagata, K., Kasagi, N., 2002. Highly energy-conservative finite-difference method for the cylindrical coordinate system. J. Comput. Phys. 181, 478–498.
Gomez, L., Mohan, R., Shoham, O., 2004. Swirling gas–liquid two-phase flow – experiment and modeling – Part I: swirling flow field. J. Fluid Eng. – T ASME 126, 935–942.
Kitoh, O., 1991. Experimental study of turbulent swirling flow in a straight pipe. J. Fluid Mech. 225, 445–479.
Klujszo, L.A., Rafaelof, M., Rajamani, R.K., 1999. Dust collection performance of a swirl cleaner. Powd. Technol. 103, 130–138.
Kuerten, J.G.M., van Kemenade, H.P., Brouwers, J.J.H., 2005. Numerical study of the rotational phase separator sealing impeller. Powd. Technol. 154, 73–82.
Lund, T.S., Wu, X., Squires, K.D., 1998. Generation of turbulent inflow data for spatially-developing boundary layer simulations. J. Comput. Phys. 140, 233–258.
Marchioli, C., Soldati, A., 2002. Mechanisms for particle transfer and segregation in turbulent boundary layer. J. Fluid Mech. 468, 283–315.
Marchioli, C., Giusti, A., Salvetti, M.V., Soldati, A., 2003. Direct numerical simulation of particle wall transfer and deposition in upward turbulent pipe flow. Int. J. Multiphase Flow 29, 1017–1038.
Marchioli, C., Salvetti, M.V., Soldati, A., 2008a. Some issues concerning large-eddy simulation of inertial particle dispersion in turbulent bounded flows. Phys. Fluids 20, 040603-1.
Marchioli, C., Soldati, A., Kuerten, J.G.M., Arcen, B., Taniere, A., Goldensoph, G., Squires, K.D., Cargnelutti, M.F., Portela, L.M., 2008b. Statistics of particle dispersion in direct numerical simulations of wall-bounded turbulence: results of an international collaborative benchmark test. Int. J. Multiphase Flow 34, 879–893.
Muntean, S., Ruprecht, A., Susan-Resiga, R., 2005. A Numerical Investigation of the 3D Swirling Flow in a Pipe with Constant Diameter. Part 2: Turbulent Computation. Scientific Bulletin of the Politehnica University of Timisoara, Transactions on Mech.
Nieuwstadt, F.T.M., Dirkzwager, M., 1995. A fluid mechanics model for an axial cyclon separator. Ind. Eng. Chem. Res. 34, 3399–3404.
Nygard, F., Andersson, H.I., 2010. DNS of swirling turbulent pipe flow. Int. J. Numer. Meth. Fluids 64, 945–972.
Orlandi, P., 2000. Fluid Flow Phenomena. A Numerical Toolkit. Kluwer Academic Publishers, London.
Orlandi, P., Fatica, M., 1997. Direct simulations of turbulent flow in a pipe rotating about its axis. J. Fluid Mech. 343, 43–72.
Parchen, R.R., Steenbergen, W., 1998. An experimental and numerical study of turbulent swirling pipe flows. J. Fluid Eng. 120, 54–61.
Pashtrapanska, M., Jovanovic, J., Lienhart, H., Durst, F., 2006. Turbulence measurements in a swirling pipe flow. Exp. Fluids 41, 813–827.
Peng, W., Hoffmann, A.C., Dries, H., 2004. Separation characteristics of swirl-tube dust separators. AIChE J. 50, 87–96.
Pettersson, B.A., Andersson, H.I., Brunvoll, A.S., 1998. Modeling near-wall effects in axially rotating pipe flow by elliptic relaxation. AIAA J. 36, 1164–1170.
Picciotto, M., Marchioli, C., Reeks, M.W., Soldati, A., 2005. Statistics of velocity and preferential accumulation of micro-particles in boundary layer turbulence. Nucl. Eng. Des. 235, 1239–1249.
Reeks, M.W., 1983. The transport of discrete particles in inhomogeneous turbulence. J. Aerosol Sci. 14, 729.
Saffman, P.G., 1965. The lift on a small sphere in a slow shear flow. J. Fluid Mech. 22, 385–400.
Saffman, P.G., 1968. The lift on a small sphere in a slow shear flow. Corrigendum 31, 624.
Sbrizzai, F., Verzicco, R., Soldati, A., 2009. Turbulent flow and dispersion of inertial particles in a confined jet issued by a long cylindrical pipe. Flow Turb. Combust. 82, 1–23.
Schiller, V.L., Naumann, A., 1935. Uber die grundlegenden Berechnungen bei der Schwerkraftaufbereitung. Z. Ver. Deut. Ing. 77, 318–320.
Soldati, A., 2005. Particles turbulence interactions in boundary layers. ZAMM – J. Appl. Math. Mech. 85, 683–699.
Soldati, A., Marchioli, C., 2009. Physics and modeling of turbulent particle deposition and entrainment: review of a systematic study. Int. J. Multiphase Flow 35, 827–839.
Soldati, A., Casal, M., Andreussi, P., Banerjee, S., 1997. Lagrangian simulation of turbulent particle dispersion in electrostatic precipitators. AIChE J. 43, 1403–1413.
Speziale, C.G., Younis, B.A., Berger, S.A., 2000. Analysis and modelling of turbulent flow in an axially rotating pipe. J. Fluid Mech. 407, 1–26.
Steenbergen, W., Voskamp, J., 1998. The rate of decay of swirl in turbulent pipe flow. Flow Meas. Instrum. 9, 67–78.
van Esch, B.P.M., Kuerten, J.G.M., 2008. Direct numerical simulation of the motion of particles in rotating pipe flow. J. Turbul. 9, 1–17.
Verzicco, R., Orlandi, P., 1996. A finite-difference scheme for three-dimensional incompressible flows in cylindrical coordinates. J. Comput. Phys. 123, 402–414.
Zhao, L., Marchioli, C., Andersson, H., 2012. Stokes number effects on particle slip velocity in wall-bounded turbulence and implications for dispersion models. Phys. Fluids 24, 021705-1.
Zonta, F., Marchioli, C., Soldati, A., 2008. Direct numerical simulation of turbulent heat transfer modulation in micro-dispersed channel flow. Acta. Mech. 195, 305–326.
Zonta, F., Marchioli, C., Soldati, A., 2011. Time behavior of heat fluxes in thermally coupled turbulent dispersed particle flows. Acta. Mech. 218, 367–373.